Cation-controlled assembly, activity, and organisation of biomimetic DNA receptors in synthetic cell membranes

Elita Peters,[1] Diana A. Tanase,[1] Lorenzo Di Michele,[1,2,3,*] and Roger Rubio-Sánchez[1,3,†]

[1]*Department of Chemical Engineering and Biotechnology, University of Cambridge, Philippa Fawcett Drive, Cambridge CB3 0AS, United Kingdom*
[2]*Department of Chemistry, Molecular Sciences Research Hub, Imperial College London, London W12 0BZ, United Kingdom*
[3]*fabriCELL, Molecular Sciences Research Hub, Imperial College London, London W12 0BZ, United Kingdom*

Biological cells use cations as signalling messengers to regulate a variety of responses. Linking cations to the functionality of synthetic membranes is thus crucial to engineering advanced biomimetic agents, such as synthetic cells. Here, we introduce bio-inspired DNA-based receptors that exploit non-canonical G-quadruplexes for cation-actuated structural and functional responses in synthetic lipid membranes. Membrane confinement grants cation-dependent control over receptor assembly and, when supplemented with hemin co-factors, their peroxidase DNAzyme activity. Cation-mediated control extends to receptor lateral distribution to localise DNA-based catalysis within phase-separated membranes domains of model synthetic cells, imitating the localisation of multimeric membrane complexes to signalling hubs in living cells. Our strategy paves the way for engineering cation-responsive pathways for sensing, signalling, and communication in synthetic cellular systems.

INTRODUCTION

Cell membranes possess specialised mechanisms to detect and transduce environmental cues to coordinate cellular responses [1]. Signal transduction pathways commonly rely on membrane receptors assembling multimeric complexes and/or undergoing conformational changes, which triggers downstream functionality through membrane-hosted reactions, e.g. (de)phosphorylation [2]. Cations, like calcium [3, 4] and potassium [5], are central to cellular signaling, typically shuttled across biological membranes as messengers to link physico-chemical stimuli to responses as varied as synaptic activation [6], muscle contraction [7], and cellular motility [8].

Synthetic cell science aims to build cell-like agents that replicate some of the intricate behaviours observed in living matter [9, 10]. Synthetic cells thus provide bottom-up platforms to dissect fundamental biological processes [11] and to unlock disruptive applications in healthcare and biotechnology [12]. By borrowing concepts and building blocks from biological and inorganic sources, solutions to engineer synthetic cells have achieved a wide range of life-like functionalities, from reconstituting cytoskeletal support [13–15] to sustaining directional motion [16, 17] to membrane-based energy harvesting [18] and mechanochemical sensing [19].

Particularly promising for the construction of human-made mimics of cells are the tools of nucleic acid nanotechnology [20, 21], as they provide robust design rules to engineer both structural and functional elements of synthetic cells. DNA and RNA nanostructures have been developed as replicas of cytoskeletal fibres [22, 23] and membrane-less organelles [24–27], or interfaced with lipid membranes [28, 29]. Amphiphilic DNA nanostructures have been applied to synthetic-cell membranes to program several biomimetic responses [30–32], ranging from molecular sensing [33] to tissue formation [34, 35] to surface [36, 37] and transmembrane [38–40] transport to bilayer remodelling [41, 42] and vesicular fission pathways [43].

Given the central role of cation homeostasis in health and disease, biomimetic devices that grant structural and functional responsiveness to cations are highly desirable, as they could help realise the fundamental and applied potential of synthetic cells. However, despite recent developments [44–46], pathways for embedding responsiveness to cations in bio-inspired systems, and particularly synthetic cell membranes, are still scarce. In the context of DNA nanotechnology, cation-stabilised G-quadruplexes (G4s), studied in biology as transcription regulators [47, 48], represent a convenient motif to engineer nano-devices with cation-controlled responses [49–51].

Here, we introduce biomimetic DNA-based membrane receptors with structural and functional responsiveness to physiologically-relevant cations. By interfacing cholesterol-modified DNA nanostructures with intermolecular G-quadruplexes, we present a membrane bio-engineering strategy to modulate the formation of receptors on the surface of lipid bilayers through independent design criteria, namely the guanine content and choice of cationic conditions. We supplemented our cation-controlled receptors with hemin co-factors to host and regulate DNAzyme peroxidase reactions on lipid membranes. Finally, we exploit DNA receptor assembly

to localise their peroxidase activity within lipid domains of phase-separated synthetic cell membranes. Our platform thus enables cation-actuated structural and functional responses in the membranes of synthetic cellular agents, paving the way for sophisticated biomimetic platforms towards signalling, molecular transport, and division.

RESULTS AND DISCUSSION

G4s assemble cation-stabilised DNA membrane receptors

Our DNA nano-devices consist of 56 base-pair (bp) long duplexes composed of four synthetic DNA oligonucleotides, featuring a terminal overhang with six consecutive guanines, $(G)_6$, that allow for receptor assembly via an intermolecular G-quadruplex [44].

As depicted in Fig. 1a, we produced $\sim 100\,\mathrm{nm}$ Large Unilamellar Vesicles (LUVs) with DOPC lipids and decorated their membranes with our nanostructures, which host double-cholesterol (dC) 'anchors' able to insert into the hydrophobic core of the bilayer [53]. Membrane functionalisation was carried out in buffered solutions containing $1\times$TE + 100 mM KCl + 87 mM sucrose, thus favouring G-quadruplex formation (see Experimental Section). Dynamic light scattering (DLS) measurements in Fig. 1b at the various LUV functionalisation stages show the expected increase in hydrodynamic diameter resulting from the membrane-tethered DNA nanostructures with and without G-rich strands. Cryo-electron microscopy, as seen in representative micrographs in Fig. 1c and Fig. S1, shows membrane-bound G-quadruplexes, which manifest as electron-dense regions [52] that are absent in LUVs decorated with nano-devices lacking the G-rich strand (Fig. S2). Circular dichroism (CD) spectra of of $(G)_6$-DNA-decorated LUVs show peaks shifts towards characteristic maximum ($\lambda \approx 263\,\mathrm{nm}$) and minimum ($\lambda \approx 245\,\mathrm{nm}$) wavelengths (Fig. 1d), relative to LUVs decorated with DNA nanostructures lacking the G-rich sequence. These shifts suggest the presence of parallel G-quadruplexes [54] consistent with the formation of tetramolecular receptors on the membrane surface [55].

Cation-controlled receptor assembly

Having assembled receptors by cross-linking individual DNA-based membrane inclusions via G-quadruplexes, we modified our nanostructure design and functionalisation conditions to control G4 formation. Specifically, we tune the length of guanine repeats and identity of the cations, both known to alter the stability of G4s [56].

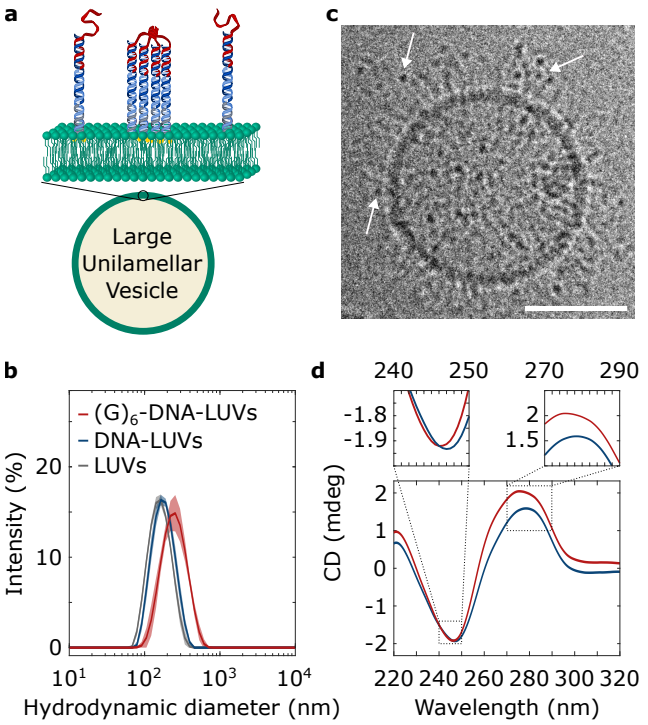

FIG. 1. **Guanine repeats in membrane-anchored DNA nano-devices guide the assembly of cation-stabilised receptors through G-quadruplexes.** **a** Schematic depiction of lipid bilayers functionalised with DNA nanostructures featuring a G-rich overhang that assembles into intermolecular G-quadruplexes stabilised by cations. **b** Hydrodynamic diameter ± standard deviation of n = 3 measurements obtained through dynamic light scattering of Large Unilamellar Vesicles (LUVs) lacking or featuring DNA nano-devices with or without the G-rich strand that supports G-quadruplex formation. **c** Cryo-electron micrograph of representantive LUV functionalised with DNA nano-devices linked to G-quadruplexes, which appear as electron-dense regions [52] (highlighted with white arrows). Scale bar = 50 nm. **d** Circular dichroism (CD) spectra of LUVs decorated with DNA nanostructures featuring either $(G)_6$-overhangs (red) or lacking the G-rich sequence (blue).

We functionalised LUVs with DNA nano-devices featuring overhang variants $(G)_{n=4,5,6}$ (Fig. 2a) in buffered solutions with added physiologically-relevant monovalent (K^+, Na^+, Li^+) or divalent (Ca^{2+}, Mg^{2+}) cations. To assess G-quadruplex formation, we exploited the fluorescence enhancement of *N*-methyl mesoprophyrin IX (NMM) when bound to parallel G-tetrads [44, 57]. As schematically depicted in Fig. 2b, we used NMM fluorimetry to compare the presence of membrane-bound G-quadruplexes with G4s assembled in the bulk from non-cholesterolised nanostructures at a nominally equal concentration ($[(G)_n] = 0.4\,\mu$M, at a DNA/lipid molar ratio of $\sim 8 \times 10^{-4}$). Owing to their tetrameric stoichiome-

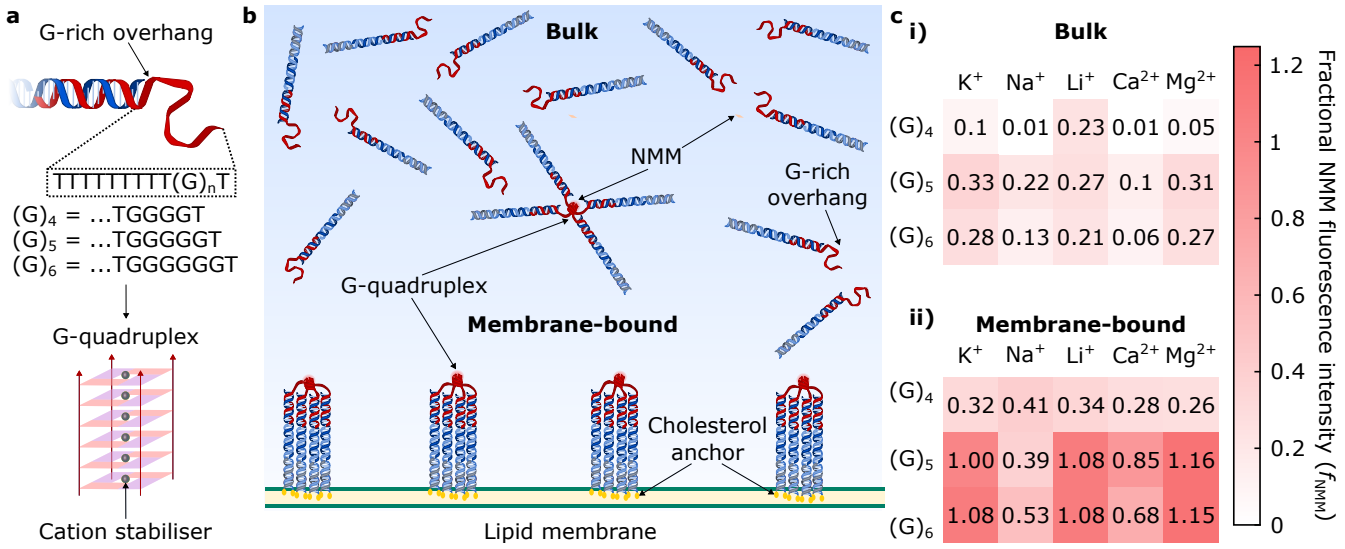

FIG. 2. **Membrane-confinement grants control over G-quadruplex formation.** **a** Schematic representation of the G-rich overhang (in red) linked to DNA nano-devices, highlighting the sequence for each design variant (G_4, G_5, and G_6), which can assemble into intermolecular, parallel, G-quadruplexes stabilised by cations. **b** Graphical depiction of tetramolecular receptors assembled through G-quadruplexes in the bulk and when membrane-bound via double-cholesterol anchors. Parallel G-tetrads selectively bind NMM and enhance its fluorescence, enabling the monitoring of the abundance of G-quadruplexes. **c** Fractional NMM fluorescence intensity (f_{NMM}) heatmaps (see Fig. S6 for the associated standard deviation δf_{NMM}) summarising the relative abundances of receptors in: i) the bulk and ii) membrane-bound as a function of monovalent (K^+, Na^+, or Li^+) and divalent (Ca^{2+} or Mg^{2+}) cations for designs G_4, G_5, and G_6 (at a nominal concentration of $[(G_n)] = 0.4\,\mu$M).

try [55], oligonucleotide concentration is expected to have a large impact on the formation of intermolecular G4s. We therefore anticipate differences in the abundance of G-quadruplexes in the bulk relative to those tethered to LUVs, where confinement to membrane surfaces increases the effective local nanostructure concentration.

To quantify the relative abundance of G-quadruplexes, we compute a fractional NMM fluorescence intensity (f_{NMM}), defined as the background-subtracted average intensity of DNA-decorated LUVs normalised by the NMM fluorescence intensity of $(G)_5$-DNA-LUVs in K^+ (see Experimental Section). The latter was chosen as it is the condition in which we found the highest fraction of G4s when nanostructures were allowed to assemble in the bulk via thermal annealing at high concentrations ($[(G)_n] = 6\,\mu$M), as quantified with agarose gel electrophoresis (Fig. S3) and observed with NMM fluorimetry (Fig. S4). Note that representative, time-invariant, fluorescent profiles in Fig. S5 confirm that both G-quadruplex formation and NMM stacking onto G-tetrads have reached thermodynamic equilibrium.

When the nanostructures were dispersed in the bulk, f_{NMM} values ≤ 0.33 shown in Fig. 2c-i (and their comparatively high standard deviation, δf_{NMM}, in Fig. S6) suggest low G4 abundance relative to DNA-decorated LUVs. Indeed, tethering our nano-devices to lipid membranes, and thus increasing their effective local concentration, led to systematically higher f_{NMM} values across the tested G-run lengths and cationic conditions (Fig. 2c-ii), confirming the expected effect on G4 assembly. The shortest G-repeat, $(G)_4$, with low f_{NMM} values – albeit higher than their bulk counterparts (with the exception of Li^+) – has relatively low G-quadruplex abundances compared to LUVs decorated with $(G)_5$ in KCl, where $f_{\mathrm{NMM}} \equiv 1$. CD signatures of $(G)_4$-decorated LUVs in K^+ show slight characteristic peak shifts (Fig. S7), consistent with the parallel quadruplex topologies observed for LUVs carrying $(G)_6$- (Fig.1c) and $(G)_5$-overhangs (Fig. S8).

Various cationic compositions, namely Li^{2+} and Mg^{2+}, enable G4 formation in $(G)_5$- and $(G)_6$ constructs to a comparable degree to that of $(G)_5$-membranes with K^+ (reaching $f_{\mathrm{NMM}} \sim 1$ and within the experimental error in Fig. S6). Similarly, DNA-decorated LUVs in Ca^{2+} have f_{NMM} values moderately lower than 1, suggesting favourable G4 formation. Interestingly, $(G)_6$- and $G)_5$-runs in the presence of Na^+ show the lowest relative abundance, with $f_{\mathrm{NMM}} \sim 0.53$ and $f_{\mathrm{NMM}} \sim 0.39$, respectively. In view of the higher G4-stabilisation expected to occur with Na^+ cations compared to Mg^{2+} or Li^+[56], the differences in G4 stability seen for DNA-LUVs are likely a consequence of membrane tethering.

We thus argue that the trends in Fig. 2c-ii may also emerge from the interplay between DNA-DNA and DNA-lipid interactions. Indeed, each cation species has a distinct affinity for phosphate groups present on both DNA and PC lipid headgroups. Cations have been shown on DNA-lipid systems to screen Coulomb interactions

and/or mediate bridging to different extents, thus inducing differences on the membrane attachment of DNA nanostructures. [45]. It is thus possible, for instance, that divalent cations further increase nanostructure effective concentration (and favour G4 formation) by bridging membranes with DNA duplexes. [45, 46]

To gain insight on the assembly dynamics of our receptors, we decorated LUV membranes with nano-devices in the presence of KCl but lacking the G-rich strand, thus preventing G4s. We subsequently added a mixture of stoichiometrically-adjusted $(G)_6$- or $(G)_5$-strands and NMM, allowing oligonucleotides to rapidly diffuse, hybridise with membrane-bound nanostructures, and assemble into K^+-stabilised G-quadruplexes where NMM could stack, leading to fluorescence enhancement (see Experimental Section). Consistent with the high local concentrations of DNA nanostructures upon membrane-confinement (estimated on Supplementary Note I to be $\sim 170\,\mu$M), NMM fluorescent profiles in Figs. S9 and S10 suggest fast G-quadruplex assembly. Equilibration of fluorescence under 250 seconds for both design variants is likely limited by the diffusion of single-stranded oligonucleotides throughout the samples, as we expect the diffusion timescales of free oligonucleotides in solution (at the relevant concentrations and lengths) [58] to be on the order of hundreds of seconds.

Cation-actuated DNA receptors with membrane-hosted catalytic activity

Our platform to control the formation of cation-stabilised receptors can be linked to the functionality of DNAzymes underpinned by G4s. A prominent example is that of the horseradish peroxidase (HRP)-mimicking DNAzyme, composed of hemin co-factors stacked onto G-tetrads [59]. Binding to G4s strongly enhances the catalytic activity of hemin when converting AmplexRed (AR) to fluorescent resorufin in the presence of hydrogen peroxide (H_2O_2) [60].

We thus produced LUVs decorated with our nano-devices and incubated them with hemin co-factors, resulting in receptor assembly hosting the HRP-mimicking DNAzyme (Fig. 4a). As shown in Fig. 3b and Figs. S11 and S12, we monitored resorufin production by means of fluorescence spectroscopy. In view of the trends summarised in Fig. 2, we expect our various designs and cationic conditions to result in different amounts of receptors available for hemin to bind, and thus the various conditions to produce differences in peroxidation rates.

To quantify the influence of our assembly platform on resorufin production, we extracted the initial reaction rates (k_{t_0}) from linear fitting of the fluorescent traces (see inset Fig. 3b and Methods) and computed their fold enhancement relative to LUVs lacking G4s in the presence

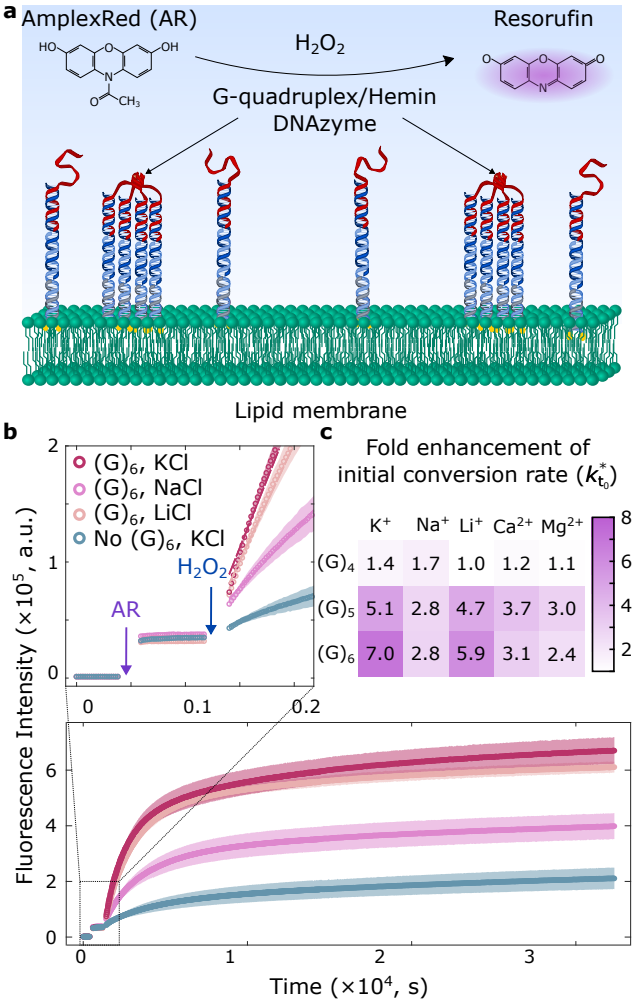

FIG. 3. **Cation-controlled DNA receptors for membrane-hosted peroxidase activity. a** Schematic depiction showing the incorporation of hemin co-factors that bind G-tetrads and form the horseradish peroxidase mimicking DNAzyme, which in the presence of hydrogen peroxide (H_2O_2) catalyses the conversion of AmplexRed (AR) to fluorescent resorufin. **b** Representative resorufin fluorescence intensity profiles of DNA-decorated LUVs with and without $(G)_6$-rich strands and added hemin co-factor in KCl, NaCl, and LiCl. The inset shows, at early times, the fluorescence intensity of LUVs before/after the addition of AR, and its increase upon initiating the reaction with H_2O_2. Solid lines are linear fits used to extract the initial rate of the reaction (k_{t_0}). **c** Heatmap of fold change in the initial rate of reaction ($k^*_{t_0} = k_{t_0,\mathrm{DNAzyme}}/k_{t_0,\mathrm{Hemin}}$) for tetramolecular DNA receptors asssembled from design variants $(G)_{n=4,5,6}$ as a function of cationic conditions.

of hemin co-factors using $k^*_{t_0} = k_{t_0,\mathrm{DNAzyme}}/k_{t_0,\mathrm{Hemin}}$. The heatmap in Fig. 3c (and the associated propagated uncertainty $\delta k^*_{t_0}$ in Fig. S13) readily confirms that various conversion rates can be accessed by design. Note that LUVs functionalised in the presence of LiCl result in higher $k^*_{t_0}$ values compared to NaCl, consistent with

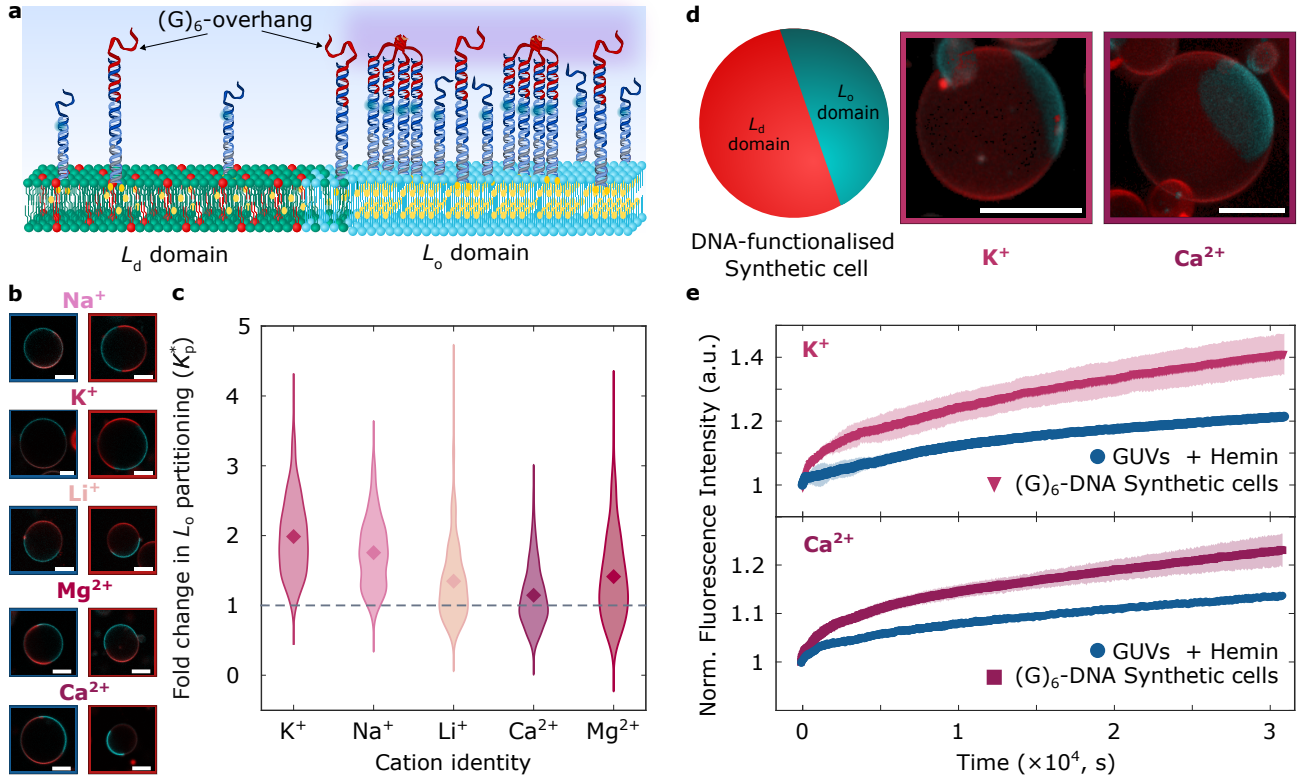

FIG. 4. **Cation-dependent assembly localises receptors and their peroxidase activity in lipid domains of synthetic cell membranes.** **a** Schematic of the organisation in lipid domains of DNA nano-devices with and without $(G)_6$-strands, and therefore, the possibility of receptor assembly localising peroxidase activity when supplemented with hemin co-factors. **b** Representative confocal equatorial micrographs of GUVs functionalised with DNA nano-devices lacking (left, framed in blue) and featuring (right, framed in red) $(G)_6$-strands to support receptor formation in buffered solutions with added monovalent (Na^+, K^+, or Li^+) or divalent (Mg^{2+}, or Ca^{2+}) salts. The TexasRed-DHPE signal, staining the L_d phase, is shown in red, while that of fluorescein (FAM)-labelled DNA nanostructures is shown in black. **c** Violin plots of the fold change in L_o-partitioning (K_p^*), computed from confocal micrographs (see Experimental Section) of DNA-decorated GUVs in either monovalent (Na^+, K^+, or Li^+) or divalent (Mg^{2+}, or Ca^{2+}) cationic conditions, showing the cation-dependent membrane distribution of DNA receptors. Diamonds are mean fold change values, while the dashed line denotes no change ($K_p^* = 1$).**d** Schematic depiction of a DNA-decorated synthetic cell (left) and 3D views of reconstructions (obtained from Volume Viewer, FIJI [61]) from confocal z-stacks of representative DNA-decorated GUVs (in the presence of K^+ or Ca^{2+}) as synthetic cell models with L_o-localised functionality. **e** Normalised fluorescence profiles monitoring resorufin production from DNA-functionalised synthetic cells in the presence of K^+ (top) or Ca^{2+} (bottom) relative to GUVs lacking DNA functionalisation but supplemented with the hemin co-factor, showing the possibility to localise peroxidase activity in lipid domains of synthetic cell membranes. All scale bars = $10\,\mu$m.

our observations in Fig. 2c)ii on higher G4 relative abundances. In contrast, while reaching high f_{NMM} values, the fold rate enhancement was systematically lower in the presence of divalent cations. We ascribe this decrease to a lower catalytic efficiency of hemin in the presence of divalent cations, as seen in the fluorescent traces on Figs. S11 and S12 where peroxidation is catalysed solely by the co-factor.

Localising receptor activity in membrane domains of synthetic cells

The cation-dependent assembly and activity of our DNA receptors can be readily coupled to membrane phase separation. Their synergy in turn enables to mimic the re-organisation and activity of multimeric protein nanomachines within cellular membrane domains.

To exemplify the applicability of our platform for synthetic-cell engineering, we produced Giant Unilamellar Vesicles (GUVs) as the chassis of our model synthetic cells, and decorated their membrane with our re-

ceptors. Synthetic cells, prepared from lipid mixtures containing DOPC/DPPC/Cholestanol in 2:2:1 molar ratios, displayed membrane phase separation at room temperature with co-existing liquid-ordered (L_o) and liquid-disordered (L_d) domains [62]. A fluorescent TexasRed-DHPE lipid marker was included to stain L_d phases, while our DNA nano-devices were modified to include a fluorescein probe to monitor their lateral organisation by means of confocal microscopy.

Given the partitioning of double-cholesterol anchors to lipid domains in phase-separated membranes [36, 63, 64], DNA receptor assembly enriched L_o domains by cross-linking four sets of dC anchors, as shown schematically in Fig. 4a and with representative confocal micrographs in Fig. 4b. Segmentation of confocal equatorial micrographs allowed us to assess DNA nanostructure partitioning by comparing average fluorescence intensities in L_o and L_d phases (see Supplementary Note II). Expectedly, as seen in Fig. S14, monomeric DNA nano-devices (i.e. lacking the G-rich strand) moderately accumulate in L_o domains. Subtle differences in their L_o-partitioning tendencies already emerge between added salts, further supporting our hypothesis of cations modulating electrostatic DNA-DNA and DNA-lipid interactions. Conversely, nanostructures featuring the $(G)_6$-overhang, and thus enabling G4 formation, systematically show stronger partitioning. In Fig. 4c we summarise the fold enhacement in L_o-partitioning (K_p^*) of $(G)_6$-DNA membranes against that of functionalised GUVs lacking $(G)_6$-overhangs. Mean values of $K_p^* > 1$ indicate stronger affinities for L_o domains, suggesting the presence of tetramolecular receptors and highlighting the ability to regulate membrane distribution of our receptors in a cation-dependent fashion.

We subsequently sought to localise receptor peroxidase activity in L_o domains of our synthetic cells. As proof-of-concept, we selected K^+ or Ca^{2+} as monovalent or divalent cation messengers, respectively, and incubated DNA-decorated synthetic cells (shown in Fig. 4d and Fig. S15 with representative 3D views from confocal z-stacks) with hemin co-factors. We monitored resorufin production upon triggering synthetic cell activity with H_2O_2, as summarised in Fig. 4e with normalised fluorescent profiles (as well as on Figs. S16 and S17 with individual replicate profiles), where synthetic-cell membranes featuring our receptors exhibit faster and higher conversion than membranes lacking functionalisation in the presence of the hemin co-factor. Epi-fluorescence micrographs in Fig. S18 of synthetic cells after peroxidation confirm their stability throughout the experimental timescales. Altogether, we demonstrate the possibility to localise and regulate activity within membrane domains of synthetic cells using different cation messengers.

CONCLUSIONS AND OUTLOOK

In summary, we have introduced biomimetic receptors with cation-controlled structure, catalytic activity, and distribution in synthetic cell membranes. Our membrane receptors exploit the formation of intermolecular G-quadruplexes to assemble on the surface of lipid bilayers. By exploiting the increased effective local concentrations caused by membrane confinement, we show that receptor formation can be controlled with different cations. Similarly, cation-mediated control allows us to regulate the rate of membrane-hosted reactions as exemplified with peroxidation using the HRP-mimicking DNAzyme. Finally, by interfacing our cation-actuated receptors with phase-separated membranes in GUVs, we established a link between the presence of cations and the lateral organisation of functional DNA-based membrane inclusions. We applied our nano-devices to host peroxidase activity within lipid domains of synthetic cells, thereby imitating the ability of cells to localise reactions within cell-membrane domains as hypothesised to occur during signalling cascades [65, 66].

Our strategy has direct applications in bottom-up synthetic biology to engineer advanced synthetic cell models. Because of its modularity and the versatility of DNA-nanotechnology, our cation-responsive approach to crosslink individual membrane inclusions can be readily adapted to guide the assembly of more intricate DNA and RNA origami nano-devices. Indeed, simple design changes can enable coupling the presence of cations to the formation of cortex-like platforms [67, 68] and membrane-remodelling nanostructures [42, 43], unlocking the development of cation-dependent pathways for cellular motion, trafficking, division, and bio-inspired synaptic transmission. In addition, the possibility of destabilising G-quadruplexes (e.g. with photo-induced damage [69, 70] or chelating agents [71]) paves the way for the development of sophisticated dynamic behaviours that respond to both physical and chemical stimuli.

Similarly, our DNA receptors could underpin the investigation of fundamental biological processes. One can envision our nano-devices as probes tethered to cellular membranes that can report on changes in electrochemical activity, allowing, for instance, to monitor the kinetics of cation waves [72, 73] as well as cation transport across biomembranes [74–76].

Finally, the effect of surface confinement on local concentration, as exploited here to regulate peroxidase activity, could be leveraged to influence the action of other DNAzymes, ribozymes [77] and (split) aptamers [78], many of which are typically underpinned by G4s. For instance, it could be possible to finely tune the efficiency

of Mg-dependent cleaving nanostructures [79] or the allosteric modulation of enzymatic action [80], thereby unlocking the possibility to host in (bio)membranes a wider range of reactions useful in biosensing, biotechnology, and bioengineering.

EXPERIMENTAL SECTION

Extrusion of Large Unilamellar Vesicles

Large Unilamellar Vesicles (LUVs) were prepared via extrusion as described in previous contributions [45, 46]. Briefly, glass vials were cleaned following a sonication routine with cycles of 15 minutes (2% Hellmanax III [HellmaAnalytics], isopropanol, and milli-Q water). After drying, 150 μL of 1,2-dioleoyl-sn-glycero-3-phosphocholine (DOPC, Avanti Polar Lipids) lipids (dispersed in chloroform at 25 mg mL^{-1}) were pipetted into the clean 1.5 mL glass vials and placed in a dry silica desiccator under vacuum for at least an hour; the lipids were rehydrated in solutions containing 300 mM sucrose by gentle vortexing for approximately 5 minutes. Resuspended vesicles then followed a 5× freeze-thaw cycle with liquid nitrogen to promote unilamellarity. Using an extrusion kit (Avanti Polar Lipids) assembled with Whatman filters and membranes (with pore size of 0.1 μm) purchased from Fisher Scientific, the resuspended vesicles were pushed through the set-up 31 times to improve monodispersity. Vesicles were stored at room temperature.

Electroformation of Phase-separating Giant Unilamellar Vesicles

Giant Unilamellar Vesicles, prepared in a 300 mM sucrose solutions, were produced via electroformation as done previously [36, 43, 62, 81]. Lipid mixtures contained DOPC (chain melting temperature -17°C), 1,2-dipalmitoyl-sn-glycero-3-phosphocholine (DPPC, chain melting temperature 41°C; Avanti Polar Lipids), and cholestanol (Sigma-Aldrich) at 2:2:1 molar ratios. Mixtures were doped with fluorescent TexasRed-DHPE (Invitrogen) at 0.8% molar ratio to preferentially stain L_{d} membrane domains. Subsequently, 45 μL of lipid mixtures (4 mg mL^{-1}) were gently spread on the conductive side of clean indium tin oxide (ITO) slides at 60°C. Slides were then placed under vacuum in a dry silica dessicator for ∼1 hour and subsequently assembled into an electroformation chamber using a ∼1 mm thick polydimethylsiloxane (PDMS) spacer enclosing approximately 200 μL of degassed sucrose buffer. Electroformation chambers, placed inside a preheated oven at $T > 60$°C and connected to a frequency generator via clamps, were subjected to a sinusoidal alternating current (AC) with voltage amplitude of 2 V. Electroformation was carried out at a frequency of 10 Hz for 2 hrs and then followed by 2 Hz for 1 hr. GUVs were retrieved and stored at room temperature in the dark to minimise photo-bleaching and photo-oxidation.

Design and assembly of DNA nanostructures

DNA nano-devices, designed using the NUPACK suite [82], are based on previously reported nano-devices [36, 44]. DNA oligonucleotides were purchased lyophilised (Integrated DNA Technologies [IDT] and Eurogentec), and were reconstituted to a nominal concentration of 100 μM in Tris – Ethylenediaminetetraacetic acid (EDTA) buffer (1× TE: 10 mM Tris + 1 mM EDTA, pH 8.0). The strands composing the DNA nano-devices were mixed at stoichimetric ratios and subjected to a slow quenching temperature ramp on an Alpha Cycler (PCR Max) thermal cycler (95°C down to 4°C at a rate of –0.5°C min $^{-1}$) in buffered saline solutions, containing either 1× TE + 100 mM monovalent salts (NaCl, KCl, or LiCl) or 1× TE + 2 mM divalent salts ($MgCl_2$ or $CaCl_2$).

Membrane Functionalisation with DNA nanostructures

Pre-assembled DNA nano-devices were incubated overnight with vesicles, either LUVs or GUVs (16.7 μL of DNA solution + 9.2 μL vesicle solution, in 57.4 μL of buffer resulting in an iso-osmolar mixture)[36, 43, 83]. Following overnight incubation, 8.35 μL of stoichiometrically-adjusted G-rich strands were mixed with a second correction buffer (10 μL). The mixture was gently added to the vesicles already decorated with DNA nano-devices, resulting in an iso-osmolar solution, containing either 1×TE + 87 mM of sugar (sucrose for LUVs and glucose for GUVs) + 100 mM of monovalent salt or 1×TE + 281 mM of sugar + 2 mM divalent salt, as required). Samples were then left under rotation overnight to allow for the G-rich strands to diffuse and hybridise the membrane-anchored dC modules.

Dynamic Light Scattering (DLS)

DLS measurements of DNA-decorated LUVs were performed using a Zetasizer Nano ZSP (Malvern Panalytical) with an excitation wavelength of $\lambda = 633$ nm and a scattering angle fixed at 173°. To that end, 100 μL

of each sample were loaded into a low-volume quartz cuvette. For each condition, n = 3 measurements, which themselves consisted of 12 runs, were collected.

Circular Dichroism (CD)

Circular Dichroism spectra were acquired a J-1500 CD Spectrometer (JASCO Corporation). Briefly, 150 μL of each sample were pipetted into a 1 mm path-length quartz cuvette. Spectra were acquired between 190 and 350 nm, with a 0.5 nm bandwidth and a 1 nm data pitch. Ten spectra were accumulated for each condition and automatically averaged by the spectropolarimeter software. Data processing included blank correction by subtracting the spectrum of LUVs dispersed in saline buffer with added sucrose (1×TE + 100 mM KCl + 87 mM sucrose). All plotted spectra were processed in the spectropolarimeter software via smoothing through a Savitzky-Golay routine with a convolution width of 17.

Agarose Gel Electrophoresis (AGE)

Agarose gels were prepared at 1.5% (w/v) in Tris-Borate-EDTA (TBE, Sigma-Aldrich, 89 mM Tris-borate, 2 mM EDTA, pH 8.3) buffer. The mixture was dissolved with pulsed-heating using a microwave. Subsequently, SYBR Safe DNA gel stain (Invitrogen) was added at 0.1% (v/v), and mixed through gentle swirling. Agarose was then casted to a thickness of approximately 5 mm. and allowed to set for 1 hour. The gel was subsquently placed in an electrophoresis chamber and covered with TBE. 15 μL of annealed samples were loaded onto the gel alongside a DNA reference ladder (1Kb bp GeneRuler, Thermo Scientific). A potential of 70 V (3.75 V cm^{-1}) was applied for 60 minutes. Finally, the gel was visualised with a G:BOX Chemi XX6 (SYNGENE) imager.

In conditions where G-quadruplex assembly is favoured, we observed the presence of two bands: i) one with higher electrophoretic mobility and thus migrating further in the gel, corresponding to monomeric nano-devices, and ii) a band with lower mobility, which corresponds to tetramolecular nanostructures stabilised by G-quadruplexes. To quantitatively assess the assembly tendencies, micrographs were loaded onto a custom-built pipeline to sample and extract the intensity profiles for each lane. From each profile containing two bands, the area under the intensity profile for each band was computed numerically to estimate a fractional intensity using:

$$f = \frac{A_{\text{low}}}{A_{\text{low}} + A_{\text{high}}} \tag{1}$$

where A_{low} and A_{high} are, respectively, the areas corresponding to the bands with low and high electrophoretic mobility. Fractional values f, which are proportional to the probabilities of finding a nanostructure in either the monomeric or tetramolecular state, were then used to compute the heatmap in Fig. S3.

Cryogenic Electron Microscopy (Cryo-EM)

Cryo-EM was used to visualise G-quadruplexes on the surface of lipid membranes. Briefly, Quantifoil 1.2/1.3 300 Cu mesh grids were double glow discharged, once per side with 25mA for 60 seconds. Subsequently, 3 μL of DNA-decorated LUVs were loaded onto grids in a Vitrobot 1 (Thermo Fisher Scientific) set to 4°C, 95% humidity, using 3-second blot times and -5 blot force, and then plunged into liquid ethane. Grids were clipped and transferred using liquid nitrogen. Micrographs were acquired using a Talos Arctica transmission electron microscope (Thermo Fisher Scientific) operated at 200 kV equipped with a Falcon 3 detector. Grid preparation and micrograph acquisition were performed at the CryoEM facility in the Department of Biochemistry, University of Cambridge.

Fluorimetry

Fluorescence spectroscopy was carried out using a BMG CLARIOstar Plus microplate reader using Clear-bottom, non-treated, 384 well-plates (NUNC).

Monitoring degree of receptor assembly with NMM fluorimetry

To assess the extent of G-quadruplex formation, 8.35 μL of stoichiometrically-adjusted NMM were mixed with 10 μL of our second correction buffer. The mixture was gently added to DNA-decorated LUVs, prepared as detailed in "Membrane Functionalisation with DNA nanostructures" and incubated for at least 30 minutes. Samples were then pipetted into 384 well-plates, covered with MicroAmp Optical Adhesive Film (ThermoFisher Scientific) to prevent evaporation, and allowed to equilibrate and thermalise (T = 25°C) inside the microplate reader for at least an hour. Measurements were performed using $\lambda_{\text{excitation}} = 388 \pm 15$ nm and $\lambda_{\text{emission}} = 670 \pm 15$ nm with fixed gains and focal heights,

adjusted by the instrument software in each independent repeat. Individual measurements, such as those shown in Fig. S5 with representative fluorescent profiles, consisted of acquisition for 30 cycles – each composed of 30 flashes per well with orbital averaging scanning mode (2 mm of diameter) across 30 flashes. The collected traces were then averaged to compute f_{NMM} using

$$f_{\mathrm{NMM}} = \frac{I_{\mathrm{NMM,x}} - I_{\mathrm{background}}}{I_{\mathrm{NMM,Max}} - I_{\mathrm{background}}} \tag{2}$$

where $I_{\mathrm{NMM,x}}$ is the fluorescence intensity of NMM in a given design variant and cationic condition and $I_{\mathrm{background}}$ is the background signal of NMM when dispersed in the respective buffered saline solution supplemented with sucrose. In turn, $I_{\mathrm{NMM,Max}}$ is the intensity of $(G)_5$-DNA-LUVs in KCl. We chose to normalise relative to this condition since $(G)_5$ in KCl exhibited the highest amount of G4s when non-cholesterolised nanostructures were assembled and allowed to equilibrate via thermal annealing, as seen in Figs. S3 and S4. Values and their errors (propagated from n = 6 repeats) were used to construct the heatmaps in Figs. 2 (main text), S4, and S6 to summarise the relative G4 abundances across the explored parameter space.

Assessing the kinetics of receptor assembly with NMM fluorimetry

To assess the formation kinetics of our cation-stabilised nanostructures, the experimental approach consisted of adding both NMM and the G-rich strand (dispersed in 1×TE without added salts to prevent assembly) to LUVs decorated with DNA nanostructures. In this manner, G-rich strands could diffuse and hybridise the nanodevices on the membrane surface, where G-quadruplexes could then assemble and mediate the fluorescence enhancement of NMM molecules. This approach was necessary given that cations are required for membrane-attachement of DNA nanostructures[45, 46]. Thus, after overnight incubation, DNA-decorated LUVs were mixed with a correction buffer such that the addition of 5 μL containing NMM + G-rich strands would result in isoosmolar solutions composed of 1×TE + 100 mM KCl + 87 mM sucrose. DNA-LUV samples, supplemented with the correction buffer, were pipetted into 384 well-plates, covered with MicroAmp Optical Adhesive Film (ThermoFisher Scientific) to prevent evaporation, and allowed to equilibrate and thermalise ($T = 25°$C) inside the microplate reader for at least an hour. Measurements were performed using $\lambda_{\mathrm{excitation}} = 388 \pm 15$ nm and $\lambda_{\mathrm{emission}} = 670 \pm 15$ nm on the "Enhanced Dynamic Range" mode of the instrument, which adjusted the focal height in each independent repeat. In each measurement, a cycle was defined as 20 flashes per well. DNA-LUV samples were measured for 50 cycles, followed by a brief pause for the addition of NMM + G-rich strand. Samples were then measured for 950 further cycles, thereby monitoring NMM fluorescence for a total of $\sim$ 2000 seconds ($\sim$ 30 minutes). In each independent repeat, a control background sample was also monitored, where NMM was added (but omiting the G-rich strand) to a buffered saline solution supplemented with sugar to a composition equal to that of DNA-LUV samples. Fluorescent profiles for each repeat were then processed individually, undergoing background subtraction and normalisation. Averaged fluorescent profiles monitoring the kinetics of assembly of membrane-bound $(G)_5$- and $(G)_6$-nanostructures are presented in Figs. S9 and S10, respectively.

Monitoring resorufin production

Stoichiometrically-adjusted hemin co-factor (8.35 μL), mixed with 10 μL of our second correction buffer, was gently added to DNA-decorated LUVs bearing G-rich strands (prepared as detailed in "Membrane Functionalisation with DNA nanostructures"). Samples were incubated for at least 30 minutes, and then pipetted into 384 well-plates, covered with MicroAmp Optical Adhesive Film (ThermoFisher Scientific) to prevent evaporation and allowed to equilibrate and thermalise ($T = 25°$C) inside the microplate reader for at least an hour. Measurements were performed using $\lambda_{\mathrm{excitation}} = 530 \pm 12.5$ nm and $\lambda_{\mathrm{emission}} = 590 \pm 17.5$ nm on the "Enhanced Dynamic Range" mode of the instrument, which adjusted the focal height in each independent repeat. In each measurement, a cycle was defined as 20 flashes per well. DNA-LUV samples were initially measured for 20 cycles, followed by a brief pause for the addition of AmplexRed (AR). Samples were then measured for 30 further cycles, paused for the addition of H_2O_2 to trigger peroxidation, and then measured for 950 cycles, thereby monitoring resorufin production for a total of 32035 seconds ($\sim$ 9 hours).

Fluorescent profiles, such as those shown in Figs. 3b (main text), S11 and S12, were processed to compute $k_{\mathrm{t_0}}$. To that end, the first 30 data points following the addition of H_2O_2 were subjected to linear fitting, from which the slope ($k_{\mathrm{t_0}}$) was extracted. The fold change in conversion rates observed with membrane-bound DNA receptors ($k_{\mathrm{t_0,DNAzyme}}$) was quantified relative to the peroxidation rates of hemin co-factor $k_{\mathrm{t_0,Hemin}}$ in each of the buffered saline solutions with added sucrose using

$$k^*_{\mathrm{t_0}} = \frac{k_{\mathrm{t_0,DNAzyme}}}{k_{\mathrm{t_0,Hemin}}} \tag{3}$$

and construct the heatmaps in Figs. 3c (main text) and S13.

Finally, profiles collected to monitor the activity of DNA-decorated synthetic cells (Fig. 4e) were obtained by normalising fluorescent traces from individual repeats (in Figs. S16 and S17). The profiles were normalised to the intensity values of the first data-point collected after H_2O_2 addition. Given the emission/excitation overlap of TexasRed in GUV membranes with resorufin, normalisation allowed to account for the slight differences in GUVs present at the measured well-positions and focal heights, which emerged as a consequence of sample preparation (from batch-to-batch variation and induced by flows from the addition of AmplexRed and hydrogen peroxide).

Fluorescence Microscopy of GUVs

DNA-functionalised GUVs were placed in polystyrene 96 well-plates (Greiner Bio-One) and allowed to sediment on the bottom for at least 10 minutes prior to imaging. The chambers were sealed with sticky-tape to prevent evaporation.

Confocal Microscopy

Confocal images were acquired at 1400 Hz, averaging over 10 frames, with a Leica TCS SP5 confocal microscope and an HC PL APO CORR CS 40× / 0.85 dry objective from Leica. Alexa488 (excitation maximum - 495 nm; emission maximum - 520 nm) signal was acquired exciting with an Ar-ion laser (488 nm).

Epifluorescence Microscopy

Epifluorescence micrographs were acquired after DNAzyme-induced peroxidation to assess the structural stability of our synthetic cell models. GUV-containing well plates were placed on the microscope stage, and the vesicles were allowed to equilibrate for at least ~ 10 minutes. Micrographs were acquired using a Nikon Eclipse Ti2-E inverted microscope, equipped with a digital camera (Hamamatsu ORCA-Flash4.0 V3), a tuneable light source (Lumencor SPECTRA X LED engine), and a Plan Fluor 40× 0.95 N.A. dry objective (Nikon).

DATA AND CODE AVAILABILITY

Data in support of this work, as well as MATLAB scripts used to analyse data, are available from the corresponding authors.

ACKNOWLEDGMENTS

E.P. acknowledges funding from the NanoDTC (EP/S022953/1) through the NanoFutures Scholars programme. R.R.S. acknowledges funding from the Biotechnology and Biological Sciences Research Council through a BBSRC Discovery Fellowship (BB/X010228/1). L.D.M. and D.A.T. acknowledge support from the European Research Council (ERC) under the Horizon 2020 research and innovation programme (ERC-STG No 851667 - NANOCELL). L.D.M. also acknowledges support from a Royal Society University Research Fellowship (UF160152, URF\R\221009). The authors acknowledge assistance from the CryoEM facility (D. Chirgadaze and L. Cooper) in the Department of Biochemistry, University of Cambridge.

COMPETING INTERESTS

The authors declare no competing interests.

* ld389@cam.ac.uk
† rmr44@cam.ac.uk

[1] Alberts, B. *Molecular biology of the cell.* (New York : Garland Science, 2017), sixth edit edn.
[2] Vitrac, H., Mallampalli, V. K. P. S. & Dowhan, W. Importance of phosphorylation/dephosphorylation cycles on lipid-dependent modulation of membrane protein topology by posttranslational phosphorylation. *J. Biol. Chem.* **294**, 18853–18862 (2019).
[3] Carafoli, E. Calcium signaling: A tale for all seasons. *Proc. Natl. Acad. Sci. U. S. A.* **99**, 1115–1122 (2002).
[4] Smajilovic, S. & Tfelt-Hansen, J. Calcium acts as a first messenger through the calcium-sensing receptor in the cardiovascular system. *Cardiovasc. Res.* **75**, 457–467 (2007).
[5] Shabala, S. Signalling by potassium: another second messenger to add to the list? *J. Exp. Bot.* **68**, 4003–4007 (2017).
[6] Heine, M., Heck, J., Ciuraszkiewicz, A. & Bikbaev, A. Dynamic compartmentalization of calcium channel signalling in neurons. *Neuropharmacology* **169**, 107556 (2020).
[7] Kuo, I. Y. & Ehrlich, B. E. Signaling in muscle contraction. *Cold Spring Harb Perspect Biol.* **7**, a006023 (2015).
[8] Tsai, F.-C., Kuo, G.-H., Chang, S.-W. & Tsai, P.-J. Ca2+ signaling in cytoskeletal reorganization, cell migration, and cancer metastasis. *Biomed Res. Int.* **2015**, 409245 (2015).
[9] Noireaux, V., Maeda, Y. T. & Libchaber, A. Development of an artificial cell, from self-organization to computation and self-reproduction. *Proc. Natl. Acad. Sci. U. S. A.* **108**, 3473 LP – 3480 (2011).
[10] Buddingh', B. C. & van Hest, J. C. M. Artificial Cells: Synthetic Compartments with Life-like Functionality and Adaptivity. *Acc. Chem. Res.* **50**, 769–777 (2017).

[11] Salehi-Reyhani, A., Ces, O. & Elani, Y. Artificial cell mimics as simplified models for the study of cell biology. *Experimental Biology and Medicine* **242**, 1309–1317 (2017). https://doi.org/10.1177/1535370217711441.

[12] Adamala, K. P. *et al.* Present and future of synthetic cell development. *Nat. Rev. Mol. Cell Biol.* **25**, 162–167 (2024).

[13] Tanaka, S., Takiguchi, K. & Hayashi, M. Repetitive stretching of giant liposomes utilizing the nematic alignment of confined actin. *Commun. Phys.* **1**, 18 (2018).

[14] Pontani, L.-L. *et al.* Reconstitution of an actin cortex inside a liposome. *Biophys. J.* **96**, 192–198 (2009). Doi: 10.1016/j.bpj.2008.09.029.

[15] Dürre, K. *et al.* Capping protein-controlled actin polymerization shapes lipid membranes. *Nat. Commun.* **9**, 1630 (2018).

[16] Zhang, S. *et al.* Engineering motile aqueous phase-separated droplets via liposome stabilisation. *Nat. Commun.* **12**, 1673 (2021).

[17] Kumar, B. V. V. S. P., Patil, A. J. & Mann, S. Enzyme-powered motility in buoyant organoclay/dna protocells. *Nat. Chem.* **10**, 1154–1163 (2018).

[18] Lee, K. Y. *et al.* Photosynthetic artificial organelles sustain and control ATP-dependent reactions in a protocellular system. *Nat. Biotechnol.* **36**, 530–535 (2018).

[19] Hindley, J. W. *et al.* Building a synthetic mechanosensitive signaling pathway in compartmentalized artificial cells. *Proc. Natl. Acad. Sci. U. S. A.* **116**, 16711 LP – 16716 (2019).

[20] Seeman, N. C. & Sleiman, H. F. DNA nanotechnology. *Nat. Rev. Mater.* **3**, 17068 (2017).

[21] Samanta, A., Pellejero, L. B., Masukawa, M. & Walther, A. Dna-empowered synthetic cells as minimalistic life forms. *Nat. Rev. Chem.* **8**, 454–470 (2024).

[22] Agarwal, S., Klocke, M. A., Pungchai, P. E. & Franco, E. Dynamic self-assembly of compartmentalized dna nanotubes. *Nat. Commun.* **12**, 3557 (2021).

[23] Tran, M. P. *et al.* Genetic encoding and expression of rna origami cytoskeletons in synthetic cells. *Nat. Nanotechnol.* (2025).

[24] Fabrini, G. *et al.* Co-transcriptional production of programmable rna condensates and synthetic organelles. *Nat. Nanotechnol.* **19**, 1665–1673 (2024).

[25] Stewart, J. M. *et al.* Modular rna motifs for orthogonal phase separated compartments. *Nat. Commun.* **15**, 6244 (2024).

[26] Malouf, L. *et al.* Sculpting dna-based synthetic cells through phase separation and phase-targeted activity. *Chem* **9**, 3347–3364 (2023).

[27] Bucci, J. *et al.* Enzyme-responsive dna condensates. *J. Am. Chem. Soc.* **146**, 31529–31537 (2024).

[28] Langecker, M., Arnaut, V., List, J. & Simmel, F. C. DNA Nanostructures Interacting with Lipid Bilayer Membranes. *Acc. Chem. Res.* **47**, 1807–1815 (2014).

[29] Franceschi, N. D., Hoogenberg, B., Katan, A. & Dekker, C. Engineering ssrna tile filaments for (dis)assembly and membrane binding. *Nanoscale* **16**, 4890–4899 (2024).

[30] Rubio-Sánchez, R., Fabrini, G., Cicuta, P. & Di Michele, L. Amphiphilic DNA nanostructures for bottom-up synthetic biology. *Chem. Commun.* **57**, 12725–127405 (2021).

[31] Mognetti, B. M., Cicuta, P. & Di Michele, L. Programmable interactions with biomimetic DNA linkers at fluid membranes and interfaces. *Rep. Prog. Phys.* **82**, 116601 (2019).

[32] Czogalla, A., Franquelim, H. & Schwille, P. Dna nanostructures on membranes as tools for synthetic biology. *Biophys. J.* **110**, 1698–1707 (2016).

[33] Kaufhold, W. T., Brady, R. A., Tuffnell, J. M., Cicuta, P. & Di Michele, L. Membrane Scaffolds Enhance the Responsiveness and Stability of DNA-Based Sensing Circuits. *Bioconjug. Chem.* **30**, 1850–1859 (2019).

[34] Parolini, L. *et al.* Volume and porosity thermal regulation in lipid mesophases by coupling mobile ligands to soft membranes. *Nat. Commun.* **6**, 5948 (2015).

[35] Beales, P. A. & Vanderlick, T. K. Application of nucleic acid–lipid conjugates for the programmable organisation of liposomal modules. *Adv. Colloid Interface Sci.* **207**, 290–305 (2014).

[36] Rubio-Sánchez, R., Barker, S. E., Walczak, M., Cicuta, P. & Di Michele, L. A Modular, Dynamic, DNA-Based Platform for Regulating Cargo Distribution and Transport between Lipid Domains. *Nano Lett.* **21**, 2800–2808 (2021).

[37] Schade, M. *et al.* Remote control of lipophilic nucleic acids domain partitioning by dna hybridization and enzymatic cleavage. *J. Am. Chem. Soc.* **134**, 20490–20497 (2012).

[38] Fragasso, A. *et al.* Reconstitution of Ultrawide DNA Origami Pores in Liposomes for Transmembrane Transport of Macromolecules. *ACS Nano* **15**, 12768–12779 (2021).

[39] Sobota, D., Joshi, H., Ohmann, A., Aksimentiev, A. & Keyser, U. F. Tailoring Interleaflet Lipid Transfer with a DNA-based Synthetic Enzyme. *Nano Lett.* **20**, 4306–4311 (2020).

[40] Langecker, M. *et al.* Synthetic lipid membrane channels formed by designed dna nanostructures. *Science* **338**, 932–936 (2012).

[41] Journot, C. M. A., Ramakrishna, V., Wallace, M. I. & Turberfield, A. J. Modifying Membrane Morphology and Interactions with DNA Origami Clathrin-Mimic Networks. *ACS Nano* **13**, 9973–9979 (2019).

[42] Franquelim, H. G., Khmelinskaia, A., Sobczak, J.-P., Dietz, H. & Schwille, P. Membrane sculpting by curved DNA origami scaffolds. *Nat. Commun.* **9**, 811 (2018).

[43] Rubio-Sánchez, R., Mognetti, B. M., Cicuta, P. & Di Michele, L. DNA-origami line-actants control domain organization and fission in synthetic membranes. *J. Am. Chem. Soc.* **145**, 11265–11275 (2023).

[44] Fabrini, G., Minard, A., Brady, R. A., Antonio, M. D. & Di Michele, L. Cation-responsive and photocleavable hydrogels from noncanonical amphiphilic dna nanostructures. *Nano Lett.* **22**, 602–611 (2022).

[45] Morzy, D. *et al.* Cations regulate membrane-attachment and functionality of DNA nanostructures. *J. Am. Chem. Soc.* **143**, 7358–7367 (2021).

[46] Morzy, D. *et al.* Interplay of the mechanical and structural properties of dna nanostructures determines their electrostatic interactions with lipid membranes. *Nanoscale* **15**, 2849–2859 (2023).

[47] Antariksa, N. F. & Antonio, M. D. The emerging roles of multimolecular g-quadruplexes in transcriptional regulation and chromatin organization. *Acc. Chem. Res.* **57**, 3397–3406 (2024). Doi: 10.1021/acs.accounts.4c00574.

[48] Tassinari, M., Richter, S. N. & Gandellini, P. Biological relevance and therapeutic potential of g-quadruplex structures in the human noncoding transcriptome. *Nu-*

cleic Acids Res. **49**, 3617–3633 (2021).

[49] Dong, J., O'Hagan, M. P. & Willner, I. Switchable and dynamic g-quadruplexes and their applications. *Chem. Soc. Rev.* **51**, 7631–7661 (2022).

[50] Chan, M. S. *et al.* Reversible reconfiguration of high-order dna nanostructures by employing g-quartet toeholds as adhesive units. *Nanoscale* **12**, 2464–2471 (2020).

[51] He, S., Ge, Z., Zuo, X., Fan, C. & Mao, X. Dynamic regulation of dna nanostructures by noncanonical nucleic acids. *NPG Asia Mater.* **13**, 42 (2021).

[52] Monsen, R. C., Chua, E. D., Hopkins, J., Chaires, J. & Trent, J. Structure of a 28.5 kda duplex-embedded g-quadruplex system resolved to 7.4 Å resolution with cryo-em. *Nucleic Acids Res.* **51**, 1943–1959 (2023).

[53] Pfeiffer, I. & Höök, F. Bivalent Cholesterol-Based Coupling of Oligonucletides to Lipid Membrane Assemblies. *J. Am. Chem. Soc.* **126**, 10224–10225 (2004).

[54] Del Villar-Guerra, R., Trent, J. O. & Chaires, J. B. G-quadruplex secondary structure obtained from circular dichroism spectroscopy. *Angew. Chem. Int. Ed.* **57**, 7171–7175 (2018).

[55] Mergny, J.-L., Cian, A. D., Ghelab, A., Saccà, B. & Lacroix, L. Kinetics of tetramolecular quadruplexes. *Nucleic Acids Res.* **33**, 81–94 (2005).

[56] Largy, E., Mergny, J.-L. & Gabelica, V. *Role of Alkali Metal Ions in G-Quadruplex Nucleic Acid Structure and Stability*, 203–258 (Springer International Publishing, 2016).

[57] Nicoludis, J. M. *et al.* Optimized end-stacking provides specificity of n-methyl mesoporphyrin ix for human telomeric g-quadruplex dna. *J. Am. Chem. Soc.* **134**, 20446–20456 (2012).

[58] Stellwagen, N. C., Magnusdottir, S., Gelfi, C. & Righetti, P. G. Measuring the translational diffusion coefficients of small DNA molecules by capillary electrophoresis. *Biopolymers* **58**, 390–397 (2001).

[59] Guo, Y. *et al.* A thermophilic tetramolecular g-quadruplex/hemin dnazyme. *Angew. Chem. Int. Ed.* **56**, 16636–16640 (2017).

[60] Golub, E., Freeman, R., Niazov, A. & Willner, I. Hemin/g-quadruplexes as dnazymes for the fluorescent detection of dna, aptamer–thrombin complexes, and probing the activity of glucose oxidase. *Analyst* **136**, 4397–4401 (2011).

[61] Schindelin, J. *et al.* Fiji: an open-source platform for biological-image analysis. *Nat. Methods.* **9**, 676–682 (2012).

[62] Veatch, S. L. & Keller, S. L. Separation of Liquid Phases in Giant Vesicles of Ternary Mixtures of Phospholipids and Cholesterol. *Biophys. J.* **85**, 3074–3083 (2003).

[63] Beales, P. A. & Vanderlick, T. K. Partitioning of Membrane-Anchored DNA between Coexisting Lipid Phases. *J. Phys. Chem. B.* **113**, 13678–13686 (2009).

[64] Beales, P. A., Nam, J. & Vanderlick, T. K. Specific adhesion between DNA-functionalized "Janus" vesicles: size-limited clusters. *Soft Matter* **7**, 1747–1755 (2011).

[65] Hong, S.-G. *et al.* Mechanosensitive membrane domains regulate calcium entry in arterial endothelial cells to protect against inflammation. *J. Clin. Investig.* **134** (2024).

[66] Shelby, S. A., Castello-Serrano, I., Wisser, K. C., Levental, I. & Veatch, S. L. Membrane phase separation drives responsive assembly of receptor signaling domains. *Nat. Chem. Biol.* **19**, 750–758 (2023).

[67] Wang, L., Cui, J., Tanner, J. A. & Shiu, S. C.-C. Self-assembly of dna tiles with g-quadruplex dnazyme catalytic activity for sensing applications. *ACS Appl. Bio Mater.* **5**, 3788–3794 (2022).

[68] Baumann, K. N. *et al.* Coating and stabilization of liposomes by clathrin-inspired dna self-assembly. *ACS Nano* **14**, 2316–2323 (2020).

[69] Ramos-Soriano, J. & Galan, M. C. Photoresponsive control of g-quadruplex dna systems. *JACS Au* **1**, 1516–1526 (2021).

[70] McBrayer, D., Schoonover, M., Long, K. J., Escobedo, R. & Kerwin, S. M. N-methylmesoporphyrin ix exhibits g-quadruplex-specific photocleavage activity. *ChemBioChem* **20**, 1924–1927 (2019).

[71] Aleman-Garcia, M. A., Orbach, R. & Willner, I. Ion-responsive hemin–g-quadruplexes for switchable dnazyme and enzyme functions. *Chem. Eur. J.* **20**, 5619–5624 (2014).

[72] Leybaert, L. & Sanderson, M. J. Intercellular ca2+ waves: Mechanisms and function. *Physiol. Rev.* **92**, 1359–1392 (2012).

[73] Stewart, T. A., Yapa, K. T. D. S. & Monteith, G. R. Altered calcium signaling in cancer cells. *Biochim. Biophys. Acta, Biomembr.* **1848**, 2502–2511 (2015).

[74] Fletcher, M. *et al.* Dna-based optical quantification of ion transport across giant vesicles. *ACS Nano* **16**, 17128–17138 (2022).

[75] Zou, J. *et al.* A dna nanodevice for mapping sodium at single-organelle resolution. *Nat. Biotechnol.* **42**, 1075–1083 (2024).

[76] Anees, P. *et al.* Detecting organelle-specific activity of potassium channels with a dna nanodevice. *Nat. Biotechnol.* **42**, 1065–1074 (2024).

[77] Ma, L. & Liu, J. Catalytic nucleic acids: Biochemistry, chemical biology, biosensors, and nanotechnology. *iScience* **23**, 100815 (2020).

[78] Debiais, M., Lelievre, A., Smietana, M. & Müller, S. Splitting aptamers and nucleic acid enzymes for the development of advanced biosensors. *Nucleic Acids Res.* **48**, 3400–3422 (2020).

[79] Cheng, Y., Huang, Y., Lei, J., Zhang, L. & Ju, H. Design and biosensing of mg2+-dependent dnazyme-triggered ratiometric electrochemiluminescence. *Anal. Chem.* **86**, 5158–5163 (2014).

[80] Riccardi, C., Napolitano, E., Platella, C., Musumeci, D. & Montesarchio, D. G-quadruplex-based aptamers targeting human thrombin: Discovery, chemical modifications and antithrombotic effects. *Pharmacol. Ther.* **217**, 107649 (2021).

[81] Angelova, M. I. & Dimitrov, D. S. Liposome electroformation. *Faraday Discuss. Chem. Soc.* **81**, 303–311 (1986).

[82] Zadeh, J. N. *et al.* NUPACK: Analysis and design of nucleic acid systems. *J. Comput. Chem.* **32**, 170–173 (2010).

[83] Ward, E. N. *et al.* Fast, multicolour optical sectioning over extended fields of view with patterned illumination and machine learning. *Biomed. Opt. Express* **15**, 1074–1088 (2024).